metals

MDPI

Article

A Comparative Study on the Influence of Chromium on the Phase Fraction and Elemental Distribution in As-Cast High Chromium Cast Irons: Simulation vs. Experimentation

U. Pranav Nayak [1,*], María Agustina Guitar [1] and Frank Mücklich [1,2]

[1] Department of Materials Science, Saarland University. Campus D3.3, D-66123 Saarbrücken, Germany; a.guitar@mx.uni-saarland.de (M.A.G.); muecke@matsci.uni-sb.de (F.M.)

[2] Materials Engineering Center Saarland (MECS), Campus D3.3, D-66123 Saarbrücken, Germany

* Correspondence: pranav.nayak@uni-saarland.de; Tel.: +49-681-302-70517

Received: 21 November 2019; Accepted: 19 December 2019; Published: 23 December 2019

Abstract: The excellent abrasion resistance of high chromium cast irons (HCCIs) stems from the dispersion of the hard iron-chromium eutectic carbides. The surrounding matrix on the other hand, provides sufficient mechanical support, improving the resistance to cracking deformation and spalling. Prior knowledge of the microstructural characteristics is imperative to appropriately design subsequent heat treatments, and in this regard, employing computational tools is the current trend. In this work, computational and experimental results were correlated with the aim of validating the usage of MatCalc simulations to predict the eutectic carbide phase fraction and the elemental distribution in two HCCI alloys, in the as-cast condition. Microstructural observations were carried out using optical microscopy and SEM. The chemical composition and fraction of each phase was measured by electron probe microanalysis and image analysis, respectively. In all cases, the values predicted by the pseudo-equilibrium diagrams, computed with MatCalc, were in accordance with the experimentally determined values. Consequently, the results suggest that time and resource intensive experimental procedures can be replaced by simulation techniques to determine the phase fraction and especially, the individual phase compositions in the as-cast state.

Keywords: high chromium cast irons; eutectic carbide; carbide volume fraction; chemical composition; image analysis; simulation; MatCalc; hardness

1. Introduction

High chromium cast irons (HCCIs) are alloys containing 15–30 wt. % Cr and 2.5–4 wt. % C, and belong to the Fe–C–Cr ternary system, as described in the ASTM A532 [1,2]. Other international standards such as ISO 21988:2006(E) classifies HCCIs under five different grades with Cr contents ranging from 11 to 40 wt. % [3]. They primarily contain hard eutectic carbides (EC) of the M_7C_3 type dispersed in a supportive, modifiable matrix. Although equilibrium solidification would result in a ferritic matrix, the final microstructure primarily contains an austenitic matrix indicating a non-equilibrium nature of solidification. The M_7C_3 carbides contribute to the hardness and wear resistance whereas the relatively softer matrix helps in improving the toughness of the HCCI alloy. This combination makes it an attractive choice for usage in applications demanding excellent abrasion and moderate impact resistance, such as ore crushers, pulverizing equipment, ball mill liners etc., in coal and mineral industries [4,5].

Although the matrix of an HCCI alloy can be modified by employing proper heat treatment, the EC are relatively immune to it [4,6]. Once the EC are formed during solidification, the only way to

modify them is by re-melting the cast and chemically modifying the melt by alloying and/or varying the process parameters. Over the years, the influence of several alloying elements such as Ti [7,8], Mo [9,10], W [11,12] etc., on the solidification behavior of the as-cast melt have been assessed. In all cases, the addition of alloying elements modified the eutectic carbide structure which resulted in a change in the final microstructural and mechanical behavior. Initially, the wear resistance was thought to be mainly influenced by the hardness of the material but it is now understood that a lot of factors contribute to this, such as type, volume fraction, size, and morphology of eutectic carbides, and its interaction with the host matrix [13–15]. Not only the carbide characteristics but also the chemical composition of the matrix after solidification determines, to a large extent, the efficacy of the subsequent heat treatment on the microstructural modifications [5,16,17]. For these reasons, it is imperative to evaluate the carbide characteristics and the chemical composition of each phase in the as-cast state.

In order to understand the processes that govern the materials' properties, it is essential to comprehend the phase diagram and phase equilibria for the given alloy composition. Complete phase diagrams for several binary and a few ternary systems are available but their construction becomes cumbersome with every additional element [18]. In this regard, employing computational techniques would be useful to extract valuable thermodynamic properties of the phases rather than experimentation. MatCalc (Materials Calculator), is a thermo-kinetic software package developed for the simulation of precipitation kinetics that occur during various metallurgical processes [19]. It employs the CALPHAD type database, which, currently is the only theoretical approach to carry out thermodynamic and kinetic calculations in multicomponent systems [20].

Studies combining simulation and experimentation have been previously conducted. Li et al. [21] computed the phase diagram of an HCCI alloy containing 15% Cr using Thermo-Calc software and compared the predicted precipitation sequence with differential scanning calorimetry (DSC) measurements. The results were in agreement with each other. Albertin et al. [22] successfully employed computational thermodynamics (Thermo-Calc) in analyzing several different HCCI compositions with the intention of optimizing the hardness and wear resistance after thermal treatments. Akyildiz et al. [23] used MatCalc to simulate pseudo-binary phase diagrams for two HCCI alloys with varying Mo contents. The predicted transformation temperatures were later compared to the DSC values to matching success. Moreover, the increase in the amount of $M_{23}C_6$ carbides with increasing Mo as predicted by the software was also seen in the alloy microstructure.

Having an idea of the microstructural characteristics (carbide volume fraction, phase chemical composition etc.) beforehand would be strongly beneficial in the development of the alloy and an appropriate design of the subsequent heat treatment (HT) to maximize its potential. Therefore, a thorough characterization in the as-cast state will serve as a terminus a quo for further microstructural modifications combining thermodynamic and kinetic calculations, and experimentally performing the thermal treatments.

The main objective of the current work is to validate the usage of thermodynamic simulation as an approach to determine the eutectic carbide phase fraction and the corresponding matrix, and carbide chemical compositions of HCCIs in the as-cast condition. Accordingly, two HCCI compositions (16% Cr and 26% Cr) were manufactured under similar conditions and their corresponding microstructural characterization was carried out in the as-cast state. The bulk compositions of the two materials were used as the input in the simulation software, MatCalc 6, to estimate the phase fraction and the chemical composition of the matrix and carbides, post solidification. Moreover, predictions from Matcalc were experimentally validated by image analysis (I-A) and electron probe microanalysis (EPMA). Additionally, the influence of the Cr content in the hardness of each phase and of the 'composite' itself, was evaluated using nanoindentation, Rockwell and Vickers microhardness tests.

2. Materials and Methodology

High chromium cast iron samples with varying Cr contents (approximately 16% and 26%) were manufactured in an arc furnace and casted at ~1450 °C into rectangular (Y) shaped sand molds

hardened with phenolic resin. Test samples were cut from the lower half of the test block measuring 175 × 90 × 25 mm^3 to ensure they were free from casting defects. Optical emission spectroscopy (GNR Metal Lab 75/80; G.N.R. S.r.l., Agrate Conturbia, Novara, Italy) was used to determine the bulk chemical composition of the castings. Table 1 represents the chemical composition (wt. %) along with the Cr/C ratio of both alloys. The cast samples were cut into pieces measuring 20 × 20 × 10 mm^3 using an abrasive disc and later embedded for microstructural characterization. Standard metallographic procedure was followed as described in [24].

Table 1. Bulk chemical composition (in wt. %) of the samples measured by optical emission spectroscopy. HCCI: high chromium cast irons.

Alloy	C	Cr	Mn	Ni	Mo	Si	Cu	P	S	Fe	Cr/C
16% HCCI (Sample A)	2.43	15.84	0.76	0.18	0.41	0.47	0.04	0.02	0.02	Bal.	6.5
26% HCCI (Sample B)	2.53	26.60	0.66	0.26	0.24	0.37	0.03	<0.01	0.04	Bal.	10.5

In addition to the bulk composition, the individual matrix and carbide compositions was measured by EPMA (8900 R JEOL Superprobe; JEOL, Tokyo, Japan) and the mean of 10 readings was considered. Phase identification was performed using a PANalytical Empyrean X-ray diffractometer (PANalytical B.V., Almelo, The Netherlands) coupled with a Co source, an acceleration voltage of 40 kV and a 40 mA tube current.

The polished samples were etched with three different etchants depending on the objective. Villella's reagent (1 g picric acid + 5 mL HCl + 95 mL C_2H_5OH) for general microstructure revelation [25], a modified Murakami's reagent (4 g $K_3[Fe(CN)_6]$ + 8 g KOH + 100 mL distilled water) for eutectic carbide volume fraction (% CVF) determination [26] and a solution of 10% HCl in methanol (CH_3OH) for deep etching to reveal the three dimensional (3D) structure of the eutectic carbides [27]. The specifics of the etchings is mentioned in Table 2. In all cases, the samples were immersed in the etchant for the appropriate time, rinsed with water and ethanol, and air dried.

Table 2. Etching parameters for each etchant.

Etchant	Solution Temperature	Etching Time
Vilella's	Room temperature (20 °C)	7–15 s
Modified Murakami's	60 °C	5 min
10% HCl in methanol	Room temperature (20 °C)	24 h

Microscopy observations were carried out using a LEXT OLS 4100 Olympus confocal laser scanning microscope (CLSM) (Olympus Corporation, Tokyo, Japan). It uses a laser with 405 nm wavelength and, a lateral and vertical resolution of 120 and 10 nm, respectively. The microstructures of the samples along with the 3D structure of the carbides were analysed using a FEI Helios Nanolab field emission scanning electron microscope (FE-SEM) working with an acceleration voltage of 5–15 kV and a beam current of 1.4 nA. A high sensitivity backscattered electron detector (vCD) was also used in order to obtain a better contrast between the phases. Furthermore, a Leica CTR6000 microscope (Leica Camera AG, Wetzlar, Germany) coupled with a Jenoptik CCD camera (Jenoptik AG, Jena, Germany) was used for image acquisition of the samples for % CVF determination. The % CVF was calculated after a post processing of the images using the image analysis (I-A) software, ImageJ (version 1.52p) (LOCI, UW-Madison, WI, USA) [28]. The analyzed area was the same for all the images and an average of 10–12 micrographs were considered for each sample.

Equilibrium phase diagrams for both alloys along with thermodynamic, and equilibrium phase fraction calculations were computed using MatCalc 6 software (version 6.01) (MatCalc Engineering

GmbH, Vienna, Austria) with the thermodynamic database "ME_Fe 1.2". The results were then correlated with the experimentally and numerically determined values obtained from I-A and empirical equations described in [29,30], respectively. Moreover, the chemical composition of each phase was estimated at a certain temperature range and compared with the EPMA results.

The bulk hardness of the samples was measured using the Rockwell hardness method, with a diamond indenter and a load of 150 kgf (HRC) whereas the matrix hardness was determined using the Vickers method. A Struers Dura Scan 50 microhardness tester (Struers Inc., Cleveland, OH, USA) with a load of 0.9807N (HV0.1) was used for this purpose. In both testing methods, the dwell time was 15 s and an average of 15–20 readings was considered. Nano-indentation (Hysitron TI 900 TriboIndenter; Bruker Corporation, Billerica, MA, USA) was used to calculate the hardness of the eutectic carbides (in GPa). A Berkovich tip, with a tip depth of 200 nm was used in displacement mode. A loading/unloading rate of 50 was maintained and the scan size was approximately 30 microns. Each indentation time was 2 min and the values were averaged over 10–12 readings.

3. Results and Discussion

3.1. Phase and Microstructural Analysis

Figure 1 represents the microstructure of the Sample A (16% HCCI) and Sample B (26% HCCI) as observed under CLSM and SEM. Their microstructure consisted of a network of eutectic carbides (EC) dispersed in a matrix of austenite dendrites. The EC was identified to be M_7C_3 which is consistent with previous studies [1,4,31,32].

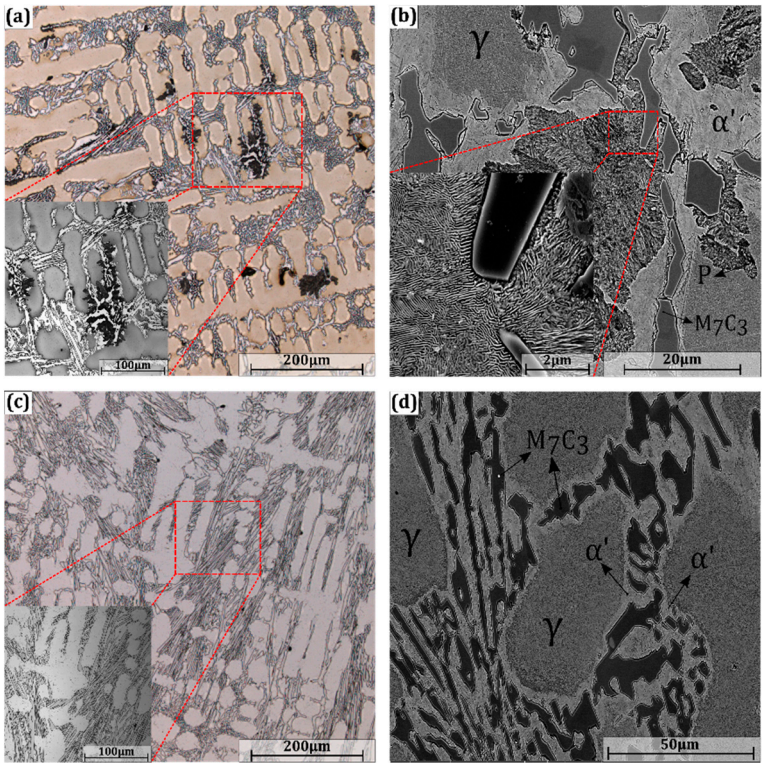

Figure 1. Representative OM (200×) and SEM micrographs of samples A (**a**,**b**) and B (**c**,**d**), respectively, after Vilella's etching. Inset in (**a**,**c**) represents a magnified image (500×) acquired using laser light. The different phases, austenite (γ), martensite (α'), pearlite (P), and eutectic carbides (M_7C_3) are indicated in images (**b**,**d**). The pearlite phase can be observed in the inset in (**b**).

From the OM and SEM micrographs, it was observed that the matrix of Sample B is completely austenitic whereas some partial transformation to pearlite has occurred in Sample A. Generally,

austenitic matrix structures are favored by high Ni and Mo contents, a high Cr/C ratio, and faster cooling rates during casting [33–35]. According to the graph presented by Maratray et al. [33], where the Cr/C ratio and the bulk Mo composition are related to the decomposition of the austenite upon cooling, for a cast alloy with a Mo content of 0.4 wt. %, the Cr/C ratio needs to be around 6.5 (which is the same as Sample A) to avoid austenite decomposition. Therefore, the partial austenite to pearlite transformation in Sample A can be primarily attributed to the low Cr/C ratio (6.5) since both samples, A and B contain negligible amounts of Ni and Mo, were casted under similar conditions, and Sample B presents a Cr/C ratio of 10.5.

In addition to the major phases, austenite and M_7C_3 EC, a thin layer of martensite was observed at the periphery of the carbides, which is clearly visible in the SEM micrographs (Figure 1b,d). The presence of these phases is further confirmed by XRD in Figure 2. The martensite formation is associated with the local C and Cr depletion which takes place during the solidification of the EC in contact with the pro-eutectic austenite, as also observed in other studies [14,24,29]. The impoverishment of alloying elements at the contact zone results in an increase in the martensitic start (M_s) temperature leading to its formation during subsequent cool down.

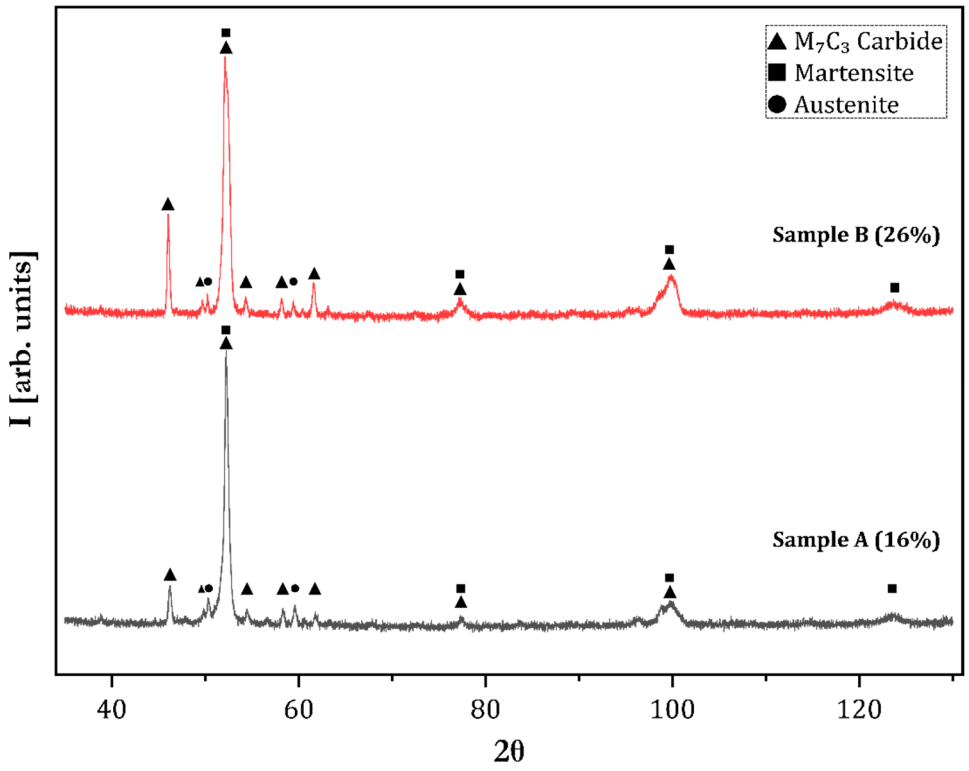

Figure 2. X-ray diffractograms of samples A and B. Austenite, martensite, and the M_7C_3 carbide are indexed for reference.

SEM micrographs depicting the three dimensional structure of the EC are shown in Figure 3. The carbides are located heterogeneously throughout the material possessing a rhombohedral/hexagonal cross section. Their growth mechanism during solidification has been explained elsewhere [31,36,37]. Both rod and plate-like EC are seen as this is a hypoeutectic alloy [15,38]. Moreover, the 'rosette' pattern can be observed in Figure 3a with hollow, fine rods at the center and larger blades as we move away. The difference in their sizes is associated with the decrease in undercooling as the solidification progresses, and the segregation of alloying elements in the melt [39].

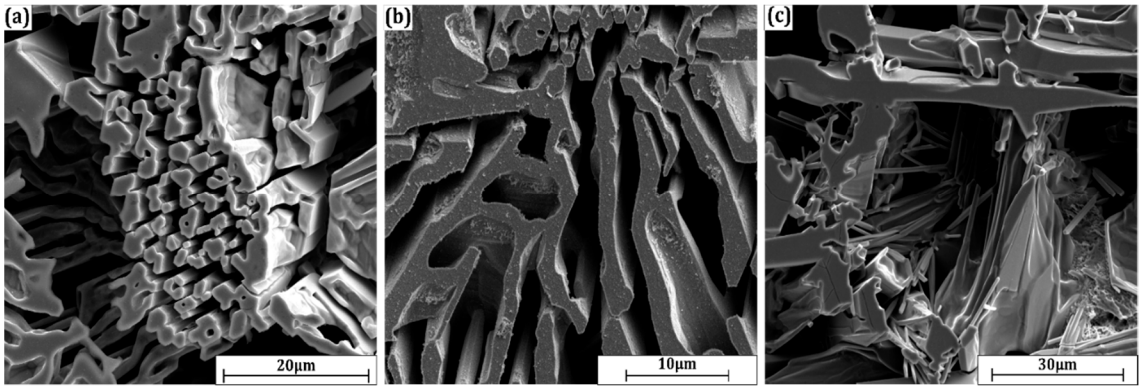

Figure 3. Representative SEM micrographs of Sample B after deep etching. The three-dimensional structure of the eutectic carbide is visible. (**a**) 'rosette' pattern, with the thin hexagonal rods at the center; (**b**) blade morphology; and (**c**) heterogenity in nucleation.

3.2. Pseudo-Binary Phase Diagram

The pseudo-binary phase diagrams for both alloys at carbon contents ranging from 2 wt. % to 5 wt. % were computed using MatCalc as shown in Figure 4. The generation of a pseudo-binary phase diagram will help in understanding the solidification sequence of the alloy and the corresponding equilibrium phase stabilities. This information is essential for alloy development and subsequent heat treatment design. From Figure 4, it can be seen that increasing the bulk chromium content results in an increase in the eutectic transition temperature (1285 → 1315 °C) and a decrease in the eutectic carbon content (3.88 wt. % → 3.24 wt. % C). Despite the similar carbon contents in the alloys, Sample B shows a smaller solidification range (30 °C) compared to its counterpart, Sample A (70 °C). It is due to the addition of chromium which increases the fraction of EC formed and improves its stability [21,23]. As a result, the formation temperature of the EC in Sample B is higher (1302 °C) in comparison with Sample A (1281 °C), indicating that it is stable for a larger range of temperatures compared to the latter. The phase diagram also predicts the formation of an additional carbide, $M_{23}C_6$, in Sample B around 1000 °C which suggests that increasing the Cr/C ratios stabilize the $M_{23}C_6$ carbide. Nevertheless, $M_{23}C_6$ was not experimentally observed, possibly due to faster cooling rate and very low Mo content [10,40].

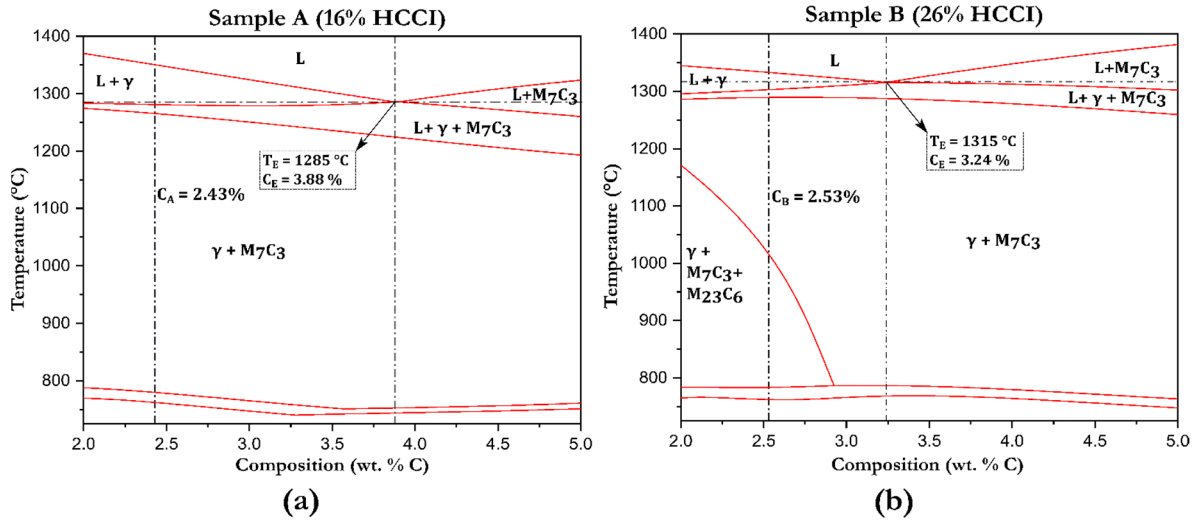

Figure 4. Pseudo-binary phase diagrams for samples, A and B computed using MatCalc 6. The eutectic transition temperature (T_E) and the corresponding eutectic carbon content (C_E) is indicated in the graphs along with the overall carbon content of (**a**) Sample A (C_A) and (**b**) Sample B (C_B).

Furthermore, to illustrate the influence of C and more specifically, Mo on the stability of the $M_{23}C_6$ carbide for various temperatures, phase boundaries were traced using MatCalc which is represented in Figure 5. It is observed, that at least 1% Mo is necessary for the low temperature stabilization of the $M_{23}C_6$ carbide at lower chromium contents for a constant carbon content, corroborating with other studies [10,41]. Moreover, at a given temperature, increasing the carbon content will necessitate an increase in the chromium content to ensure the stability of $M_{23}C_6$. This is because Cr is primarily a M_7C_3 carbide former for HCCI's up to 30% Cr after which, $M_{23}C_6$ becomes the stable carbide upon solidification [32,34].

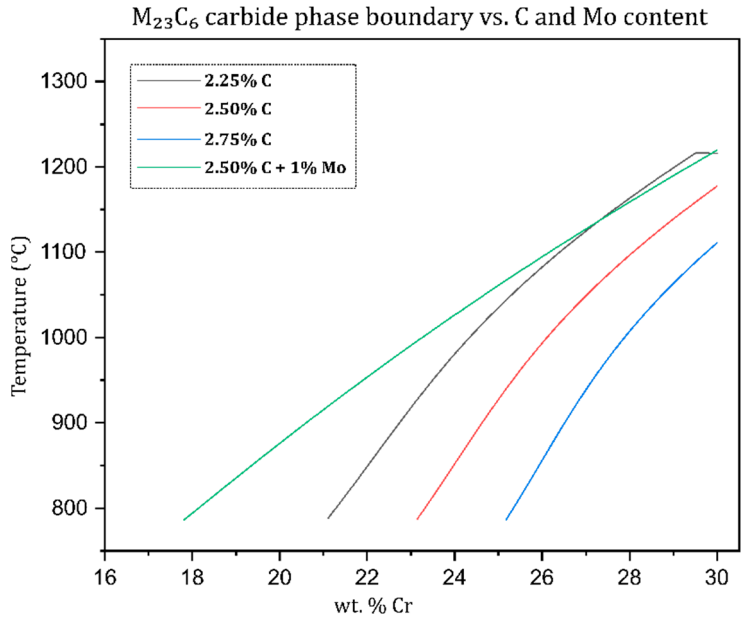

Figure 5. The influence of C and Mo on the phase boundary of the $M_{23}C_6$ carbide predicted by MatCalc 6.

3.3. Carbide Volume Fraction

It is well known that the nature and volume fraction of the EC is strongly influenced by the amount of chromium present in the alloy, as it is a strong carbide former [42]. The volume fraction of the EC corresponding to both samples, A and B was theoretically determined using empirical formulae suggested by Maratray et al. [29] (Equation (1)) and Doğan et al. [30] (Equation (2)), which was solely based on the bulk composition of C and Cr (in wt. %). Additionally, the total bulk chemical composition (Table 1) was used as the input for the software in simulating the equilibrium fraction of each phase. Figure 6 represents the equilibrium phase fractions determined for both alloys using MatCalc. The theoretical (Equations (1) and (2)) and simulated (MatCalc) values were then compared to the experimental results obtained from the I-A of microscopy images.

$$\% \text{ CVF} = 12.33\ (\%C) + 0.55\ (\%Cr) - 15.2 \quad (1)$$

$$\% \text{ CVF} = 14.05\ (\%C) + 0.43\ (\%Cr) - 22 \quad (2)$$

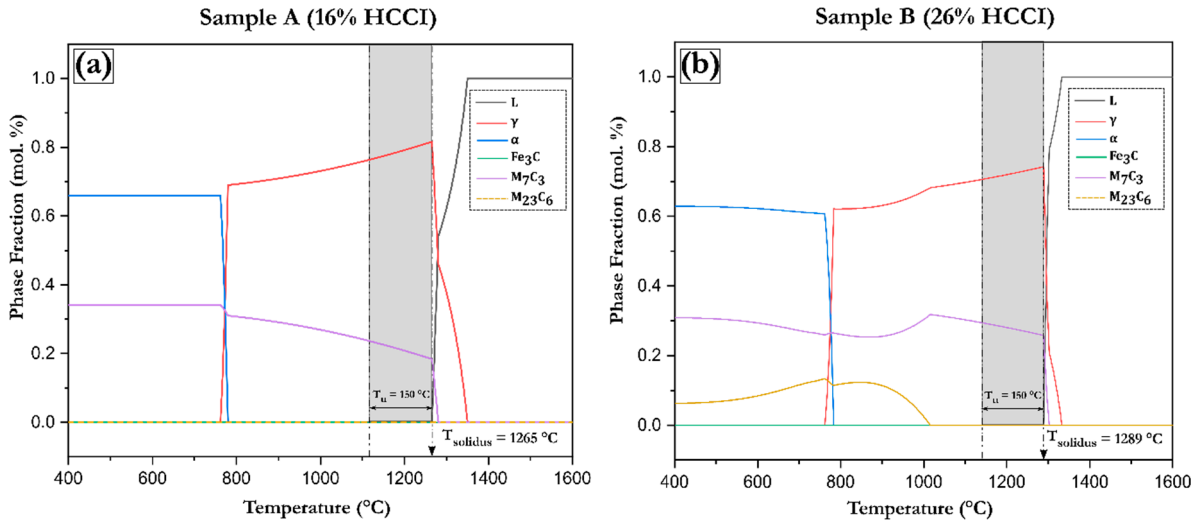

Figure 6. Equilibrium phase fractions for (**a**) Sample A (16% HCCI) and (**b**) Sample B (26% HCCI) as predicted by MatCalc. The solidus temperature, $T_{solidus}$ for both alloys including the range of undercooling considered, T_u = 150 °C is indicated in the schematic.

Table 3 compares the % CVF obtained using the different approaches. It is evident that the % CVF of Sample B is higher than Sample A owing to the increased chromium for a quasi-constant carbon content. The % CVF increased by approximately 50% for an additional 10 wt. % of chromium. The differences in the results shown by the two formulae could be due to the number of samples considered for the study and the accuracy of determining the % CVF for each alloy [29,30]. Equation (1) was deduced by Maratray et al. after studying over 40 different alloys with varying C (1.95 to 4.31 wt. %) and Cr (10.8 to 25.82 wt. %) contents. Equation (2) is a result of the work carried out by Doğan et al. on hypoeutectic, eutectic and hypereutectic cast iron compositions with Cr contents of 15 and 26 wt. %. The hypoeutectic compositions considered in [30] is analogous to the alloys used in this study. Although the experimental values are close to the numerically predicted values, care must be taken as the formulae only consider the influence of C and Cr [1].

Table 3. Comparison between the % carbide volume fractions (CVFs) of both alloys obtained using different approaches.

Sample	Emperical Formulae (%)		MatCalc (at $T_{solidus}$) (%)	MatCalc (at $T_{solidus}$ −150 °C) (%)	Experimental (I-A) (%)
	Maratray [29]	Doğan [30]			
A (16% HCCI)	23.4 ± 2.1	19.0	18.4	21.2 ± 1.5	19.4 ± 0.4
B (26% HCCI)	30.6 ± 2.1	25.0	25.8	27.7 ± 1.1	30.4 ± 0.6

The equilibrium EC phase fraction predicted by MatCalc was initially considered at the temperature where the liquid ceases to exist i.e., the solidus temperature, $T_{solidus}$. Due to the larger solidification range of Sample A, its $T_{solidus}$ is lower (1265 °C) than Sample B (1289 °C). In both cases, the % CVF predicted by MatCalc is lower than the values obtained experimentally which can be explained by the non-equilibrium solidification during casting, leading to the existence of an undercooling regime [31,39]. Considering a degree of undercooling, T_u = 150 °C, and averaging the phase fraction values in that range ($T_{solidus}$−150 °C) for both alloys yields a value of 21.2% ± 1.5% CVF for Sample A and 27.7% ± 1.1% CVF for Sample B. Comparing this % CVF with the value determined at $T_{solidus}$, an increase is observed in both cases (Sample A and Sample B). The increase in the % CVF with decreasing temperature can be attributed to the increased driving force for nucleation due to the undercooling effect. Consequently, it is observed that the predicted and experimental % CVF values correspond well and differences between them, fall within an error of less than 5%.

To further validate the results given by the simulation software, a few alloys with varying C and Cr contents were considered from the expansive study conducted by Maratray et al. [29] and Doğan et al. [30]. Table 4 lists the considered alloys and the % CVF obtained using metallography, Equations (1) and (2), and the prediction by MatCalc. The procedure employed to obtain the % CVF from MatCalc is similar to the one previously mentioned, i.e., determining the $T_{solidus}$ for each composition and considering an undercooling range, T_u = 150 °C. It is seen that for relatively low Cr/C ratios (3.7–4.3), the formula suggested by Doğan and experimental values match, whereas Maratray's formula can be used for higher Cr/C ratios. It is also worth mentioning that increasing the Cr content alone did not lead to a significant increase in % CVF as evident in alloys M1 and M3. Comparing the alloys M1, D1 and M2, it is observed that addition of C (2.08 → 3.54 → 4.10) for a relatively constant Cr led to a massive increase in the % CVF (18.7 → 33.0 → 42.0). This further consolidates the effect of C on the volume fraction of the carbides compared with Cr. Despite the drastic variation in C and Cr content in all samples, the % CVF predicted by MatCalc is always comparable to the experimentally determined values which supports the usage of simulation to predict the volume fraction of the eutectic carbide in the as-cast state.

Table 4. The % CVF of certain alloys experimentally determined by [29,30], the numerical estimations and the corresponding % CVF computed using MatCalc (in grey).

Study	Alloy	Chemical Composition (wt. %)							Cr/C	% CVF (Experiment)	% CVF Equation (1)	% CVF Equation (2)	% CVF (MatCalc)
		C	Cr	Mn	Mo	Si	Ni	Fe					
Maratray et al. [29]	M1	2.08	15.85	0.70	-	1.00	-	Bal.	7.6	18.7	19.2 ± 2.1	14.0	16.8 ± 1.5
	M2	4.10	15.10	0.70	-	1.00	-	Bal.	3.7	42.0	43.7 ± 2.1	42.1	40.9 ± 1.2
	M3	2.08	20.55	0.70	-	1.00	-	Bal.	9.9	20.5	21.7 ± 2.1	16.1	19.7 ± 1.3
	M4	2.95	25.82	0.70	0.02	1.00	-	Bal.	8.8	32.3	35.4 ± 2.1	30.6	32.3 ± 1.0
Doğan et al. [30]	D1	3.54	15.2	0.61	0.31	0.51	0.18	Bal.	4.3	33.0 ± 2.0	36.8 ± 2.1	34.3	34.0 ± 1.4
	D2	2.76	26.2	0.93	0.38	0.42	0.38	Bal.	9.5	29.0 ± 1.0	33.2 ± 2.1	28.0	30.4 ± 1.1

3.4. Chemical Composition

In order for effectively designing heat treatment cycles, it is essential to have an understanding of the individual matrix and carbide compositions [30]. The composition between the matrix and carbide will vary depending upon the alloying elements present, the cooling rate during casting and the bulk Cr/C ratio [1,5]. For these reasons, and in order to correlate experimental with simulated values, the matrix and carbide chemical composition were determined by EPMA and MatCalc (Table 5). The matrix and carbide elemental compositions determined with MatCalc, were calculated considering the weight fraction of the element present in the respective phase at the given temperature and taking the average value over the undercooling range ($T_{solidus} - T_u$).

Table 5. Matrix and carbide elemental compositions (in wt. %) for the two alloys as determined by electron probe microanalysis (EPMA) and MatCalc. The distribution of Cr and Fe within the M_7C_3 carbide is also compared.

Sample	Matrix			Carbide			$(Cr_xFe_y)C_3$	
	Element (wt. %)	EPMA	MatCalc	Element (wt. %)	EPMA	MatCalc	EPMA	MatCalc
A (16% HCCI)	C	0.86 ± 0.34	1.12 ± 0.12	C	7.54 ± 0.49	8.71 ± 0.00	$(Cr_{3.9}Fe_{3.1})C_3$	$(Cr_{3.9}Fe_{3.1})C_3$
	Cr	12.10 ± 0.21	8.79 ± 0.71	Cr	48.81 ± 3.63	49.5 ± 0.45		
	Mn	0.60 ± 0.02	0.77 ± 0.00	Mn	-	-		
	Ni	0.13 ± 0.03	0.21 ± 0.00	Ni	0	0		
	Mo	0.21 ± 0.04	0.27 ± 0.03	Mo	-	-		
	Fe	85.6 ± 0.3	88.84 ±0.85	Fe	41.99 ± 3.65	39.99 ± 0.52		
B (26% HCCI)	C	0.43 ± 0.13	0.69 ± 0.09	C	7.85 ± 0.53	8.83±0.00	$(Cr_5Fe_2)C_3$	$(Cr_5Fe_2)C_3$
	Cr	18.21 ± 1.24	15.37 ± 0.78	Cr	63.07 ± 1.87	65.13 ± 0.77		
	Mn	0.67 ± 0.03	0.72 ± 0.00	Mn	-	-		
	Ni	0.20 ± 0.04	0.33 ± 0.00	Ni	0	0		
	Mo	0.14 ± 0.03	0.2 ± 0.01	Mo	-	-		
	Fe	80.0 ± 1.3	82.68 ± 0.87	Fe	28.36 ± 2.11	25.19 ± 0.79		

From Table 5, it is evident that the Cr content (wt. %) of both the matrix and EC increased as the bulk Cr content increased although the C content (wt. %) in the EC remained at a stoichiometric level. The addition of chromium reduces the carbon solubility in austenite [17] and as a result, the 26% HCCI alloy has a lower matrix C content. This can be further elucidated by considering the partition ratio of the elements. The segregation or partition ratio, as coined by Laird [43], is the element's affinity to partition into the carbide or the matrix and can be defined as the ratio of the weight percent of the element in the carbide to the matrix. Higher ratios, as in the case of chromium and carbon suggest strong partitioning towards the carbides whereas elements such as Si, Ni, and Cu are found only at the matrix regions. The Cr partition ratio from EPMA measurements for Sample A and Sample B was 4 and 3.5, respectively. Furthermore, the partition ratio of C in Sample B (18.25) is higher compared to Sample A (8.77) indicating an increased affinity to the eutectic carbides (as evidenced by the lower C content of the 26% HCCI matrix).

The distribution of Cr and Fe within the EC was determined by converting the respective weight percentages into atomic percentage and normalizing with the carbon atomic percentage (30 at. %). Despite both materials having M_7C_3 as the EC, the Fe/Cr ratio is lower in the case of 26% HCCI indicating that less Cr atoms were substituted by Fe. It is also worthy to mention that although trace amounts of Mn and Mo were detected by EPMA and also predicted by MatCalc in the EC for both samples, it is not shown in Table 5. The Cr content (in at. %) of the EC increased from approximately 40% in Sample A to 50% in Sample B, which is the highest for these type of alloys [29]. In both cases, the elemental compositions of the matrix and EC, and the chromium–iron distribution in the EC predicted by MatCalc are in accordance with the values measured by EPMA.

A similar alloy (C, 2.72%; Cr, 26.6%; Mn, 0.2%; Si, 0.78%; Ni, 0.17%) was studied by Carpenter et al. [44] wherein the Cr content of the EC was determined to be 49.7 at. % ± 1.6 at. % by chemical microanalysis. Comparing this alloy with Sample B, it is observed that the Cr content of the EC is identical in both cases even though there is a slight increase in the bulk C content. This further upholds the notion that 50 at. % Cr ($Cr_5Fe_2C_3$) is the highest for M_7C_3 type of EC in HCCIs [33]. Moreover, the experimental value obtained by Carpenter et al. was corroborated by MatCalc, which predicted a Cr content of 49.7 at. % ± 0.7 at. % Cr in the EC.

3.5. Hardness

Table 6 details the values of hardness on three different scales. Sample B shows higher bulk hardness (HRC) owing to the higher volume fraction of the M_7C_3 carbides formed. Despite the differences in the chemical composition of the matrix, its microhardness (HV0.1) for both alloys remained similar. This coincidental value of the matrix hardness can be attributed to the presence of a high carbon matrix in Sample A and a high alloying in Sample B due to the Cr content [30]. It also sheds light on the efficacy of the carbon contribution to the hardness of the matrix compared to chromium. Furthermore, the hardness of the M_7C_3 carbide increases from Sample A to Sample B which could be attributed to the increasing Cr content of the carbide [45].

Table 6. Results of the bulk, matrix and carbide hardness for both alloys.

Sample	Rockwell (HRC) (Bulk)	Vickers (HV0.1) (Matrix)	Nanoindentation (GPa) (EC)
A (16% HCCI)	46.3 ± 0.8	356 ± 11	13.1 ± 1.7
B (26% HCCI)	49.3 ± 0.5	360 ± 21	19.0 ± 1.2

4. Conclusions

Computational tools and experimental results were combined in this work with the aim to validate the usage of MatCalc simulations for the prediction of phase fractions and elemental distribution in HCCI's in the as-cast condition, for the convincing implementation of these tools for further heat

treatment design. For that, two as-cast alloys (containing 16% and 26% Cr) were fabricated under similar conditions with the main variance being the Cr content. The EC phase fraction and the individual matrix, and carbide compositions were determined experimentally and compared with the values predicted by the MatCalc simulation. The principal conclusions that can be drawn from the above work are as follows:

- OM and SEM micrographs indicate a dispersion of M_7C_3 eutectic carbides in an austenitic matrix with a thin layer of martensite formed at the carbides' periphery for both alloys. Although the matrix is purely austenite in Sample B, some partial transformation to pearlite has occurred in Sample A, owing to the low Cr/C ratio.
- The pseudo-binary phase diagrams constructed using MatCalc indicate the formation of $M_{23}C_6$ carbide at temperatures below 1050 °C in Sample B. However, the presence of $M_{23}C_6$ carbide was not detected due to the non-equilibrium cooling and the low Mo content of the alloy.
- An addition of 10 wt. % Cr lead to an increase of about 50% of the EC as evidenced by image analysis. The % CVF was lower when determined from MatCalc at $T_{solidus}$. Nevertheless, by considering an undercooling range of 150 °C as a consequence of the non-equilibrium solidification, the predicted % CVF corresponded well with experimentally determined values. Therefore, the MatCalc simulated data is reliable for the determination of % CVF. The accuracy of the simulation software was further validated comparing the % CVF of several alloys (with different C and Cr contents) to the experimental values obtained by other authors from metallographic techniques.
- The predictions made by MatCalc are in accordance with the values obtained by EPMA. MatCalc also predicted an increase Cr/Fe ratio in the EC with increasing Cr content, which was corroborated by EPMA measurements. Additionally, the Cr/Fe ratio predicted by MatCalc for Sample B showed a good correspondence with experimental results found in the literature.
- Finally, the increase in the bulk hardness of Sample B was related to the increased M_7C_3 fraction, whereas the individual EC hardness was higher in Sample B than Sample A due to the increased Cr occupation in the EC. Despite the lower bulk and carbide hardness, the matrix hardness of Sample A was on par with B, probably due to the high C content in the matrix which prevented a decrement.

To sum up, this work demonstrated the capability of MatCalc to accurately predict the EC phase fraction and elemental distribution within the phases, which bolsters its implementation in the design of heat treatments. The time and resource intensive experimental procedures can be replaced by simulation techniques to determine the phase fraction and especially, the individual phase compositions in the as-cast state. Furthermore, the elemental distribution within the matrix and EC is reflected in its corresponding hardness. The knowledge provided by this tool about the elemental distribution within the phases beforehand will assist in designing a heat treatment cycle for an HCCI alloy to be used in a specific application and pave way for 'microstructural tailoring'. Accordingly, the microstructural modifications occurring in these alloys during heat treatments, including the carbide precipitation kinetics, will be investigated as a part of future work.

Author Contributions: Conceptualization and methodology, U.P.N. and M.A.G.; Simulation, experimental validation, formal analysis, data curation and writing–original draft preparation, U.P.N.; writing–review and editing, and supervision, M.A.G. and F.M.; project administration and funding acquisition, F.M. All authors have read and agreed to the published version of the manuscript.

Funding: The authors wish to acknowledge the EFRE Funds (C/4-EFRE-13/2009/Br) of the European Commission for supporting activities within the AME-Lab project.

Acknowledgments: The authors would like to thank Martin Duarte from Tubacero S.A. for providing the materials and Sandvik Materials Technology for the EPMA measurements. Additionally, UP Nayak is grateful to DAAD for the financial support.

Conflicts of Interest: The authors declare no conflict of interest.

References

1. Tabrett, C.P.; Sare, I.R.; Ghomashchi, M.R. Microstructure-property relationships in high chromium white iron alloys. *Int. Mater. Rev.* **1996**, *41*, 59–82. [CrossRef]
2. ASTM Standard A 532/A 532M-93a. *Standard Specification for Abrasion Resistance Cast Irons*; ASTM International: West Conshohocken, PA, USA, 2003. Available online: www.astm.org (accessed on 23 December 2019).
3. International Organization for Standardization. *Abrasion-Resistant Cast Irons-Classification (ISO 21988:2006)*; International Organization for Standardization: Geneva, Switzerland, 2006. Available online: www.iso.org (accessed on 23 December 2019).
4. Karantzalis, E.; Lekatou, A.; Mavros, H. Microstructure and properties of high chromium cast irons: Effect of heat treatments and alloying additions. *Int. J. Cast Met. Res.* **2009**, *22*, 448–456. [CrossRef]
5. Wiengmoon, A.; Pearce, J.T.H.; Chairuangsri, T. Relationship between microstructure, hardness and corrosion resistance in 20 wt. %Cr, 27 wt. %Cr and 36 wt. %Cr high chromium cast irons. *Mater. Chem. Phys.* **2011**, *125*, 739–748. [CrossRef]
6. Laird, G.; Powell, G.L.F. Solidification and solid-state transformation mechanisms in Si alloyed high-chromium white cast irons. *Metall. Trans. A* **1993**, *24*, 981–988. [CrossRef]
7. Bedolla-Jacuinde, A.; Correa, R.; Quezada, J.G.; Maldonado, C. Effect of titanium on the as-cast microstructure of a 16%chromium white iron. *Mater. Sci. Eng. A* **2005**, *398*, 297–308. [CrossRef]
8. Kopyciński, D.; Guzik, E.; Siekaniec, D.; Szczęsny, A. The effect of addition of titanium on the structure and properties of high chromium cast iron. *Arch. Foundry Eng.* **2015**, *15*, 35–38. [CrossRef]
9. Scandian, C.; Boher, C.; de Mello, J.D.B.; Rézaï-Aria, F. Effect of molybdenum and chromium contents in sliding wear of high-chromium white cast iron: The relationship between microstructure and wear. *Wear* **2009**, *267*, 401–408. [CrossRef]
10. Imurai, S.; Thanachayanont, C.; Pearce, J.T.H.; Tsuda, K.; Chairuangsri, T. Effects of Mo on microstructure of as-cast 28 wt. % Cr-2.6 wt. % C-(0-10) wt. % Mo irons. *Mater. Charact.* **2014**, *90*, 99–112. [CrossRef]
11. Lv, Y.; Sun, Y.; Zhao, J.; Yu, G.; Shen, J.; Hu, S. Effect of tungsten on microstructure and properties of high chromium cast iron. *Mater. Des.* **2012**, *39*, 303–308. [CrossRef]
12. Cortés-Carrillo, E.; Bedolla-Jacuinde, A.; Mejía, I.; Zepeda, C.M.; Zuno-Silva, J.; Guerra-Lopez, F.V. Effects of tungsten on the microstructure and on the abrasive wear behavior of a high-chromium white iron. *Wear* **2017**, *376–377*, 77–85. [CrossRef]
13. Doğan, Ö.N.; Hawk, J.A. Effect of carbide orientation on abrasion of high Cr white cast iron. *Wear* **1995**, *189*, 136–142. [CrossRef]
14. Gahr, K.H.Z.; Doane, D.V. Optimizing fracture toughness and abrasion resistance in white cast irons. *Metall. Trans. A* **1980**, *11*, 613–620. [CrossRef]
15. Asensio, J.; Pero-Sanz, J.A.; Verdeja, J.I. Microstructure selection criteria for cast irons with more than 10 wt. % chromium for wear applications. *Mater. Charact.* **2002**, *49*, 83–93. [CrossRef]
16. Maratray, F.; Poulalion, A. Austenite Retention in High-Chromium White Irons. *Trans. Am. Foundrym. Soc.* **1982**, *90*, 795–804.
17. Poolthong, N.; Nomura, H.; Takita, M. Effect of heat treatment on microstructure and properties of semi-solid chromium cast iron. *Mater. Trans.* **2004**, *45*, 880–887. [CrossRef]
18. *ASM Handbook Volume 3: Alloy Phase Diagrams*; ASM International: Materials Park, OH, USA, 2016; ISBN 978-1-62708-070-5. Available online: www.asminternational.org (accessed on 23 December 2019).
19. Kozeschnik, E.; Buchmayr, B. Matcalc—A simulation tool for multicomponent thermodynamics, diffusion and phase transformations. In Proceedings of the Mathematical Modelling of Weld Phenomena, Leibnitz, Austria, 1–3 October 2001; pp. 349–361.
20. Kroupa, A. Modelling of phase diagrams and thermodynamic properties using Calphad method—Development of thermodynamic databases. *Comput. Mater. Sci.* **2013**, *66*, 3–13. [CrossRef]
21. Li, D.; Liu, L.; Zhang, Y.; Ye, C.; Ren, X.; Yang, Y.; Yang, Q. Phase diagram calculation of high chromium cast irons and influence of its chemical composition. *Mater. Des.* **2009**, *30*, 340–345. [CrossRef]
22. Albertin, E.; Beneduce, F.; Matsumoto, M.; Teixeira, I. Optimizing heat treatment and wear resistance of high chromium cast irons using computational thermodynamics. *Wear* **2011**, *271*, 1813–1818. [CrossRef]
23. Akyildiz, Ö.; Candemir, D.; Yildirim, H. Simulation of Phase Equilibria in High Chromium White Cast Irons. *Uludağ Univ. J. Fac. Eng.* **2018**, *23*, 179–190. [CrossRef]

24. Guitar, M.A.; Scheid, A.; Suárez, S.; Britz, D.; Guigou, M.D.; Mücklich, F. Secondary carbides in high chromium cast irons: An alternative approach to their morphological and spatial distribution characterization. *Mater. Charact.* **2018**, *144*, 621–630. [CrossRef]
25. Guitar, M.A.; Suárez, S.; Prat, O.; Duarte Guigou, M.; Gari, V.; Pereira, G.; Mücklich, F. High Chromium Cast Irons: Destabilized-Subcritical Secondary Carbide Precipitation and Its Effect on Hardness and Wear Properties. *J. Mater. Eng. Perform.* **2018**, *27*, 3877–3885. [CrossRef]
26. Collins, W.K.; Watson, J.C. Metallographic etching for carbide volume fraction of high-chromium white cast irons. *Mater. Charact.* **1990**, *24*, 379–386. [CrossRef]
27. Wiengmoon, A.; Chairuangsri, T.; Poolthong, N.; Pearce, J.T.H. Electron microscopy and hardness study of a semi-solid processed 27 wt%Cr cast iron. *Mater. Sci. Eng. A* **2008**, *480*, 333–341. [CrossRef]
28. Schindelin, J.; Ignacio Arganda-Carreras, E.F.; Kaynig, V.; Longair, M.; Pietzsch, T.; Preibisch, S.; Rueden, C.; Saalfeld, S.; Schmid, B.; Tinevez, J.-Y.; et al. Fiji: An open-source platform for biological-image analysis. *Nat. Methods* **2012**, *9*, 676–682. [CrossRef]
29. Maratray, F.; Usseglio-Nanot, R. *Factors Affecting the Structure of Chromium and Chromium—Molybdenum White Irons*; Climax Molybdenum S. A: Paris, France, 1970.
30. Doğan, Ö.N.; Hawk, J.A.; Laird, G. Solidification structure and abrasion resistance of high chromium white irons. *Metall. Mater. Trans. A Phys. Metall. Mater. Sci.* **1997**, *28*, 1315–1328. [CrossRef]
31. Bedolla-Jacuinde, A.; Hernández, B.; Béjar-Gómez, L. SEM study on the M7C3 carbide nucleation during eutectic solidification of high chromium white irons. *Zeitschrift Met.* **2005**, *96*, 1380–1385.
32. Zumelzu, E.; Goyos, I.; Cabezas, C.; Opitz, O.; Parada, A. Wear and corrosion behaviour of high-chromium (14–30% Cr) cast iron alloys. *J. Mater. Process. Technol.* **2002**, *128*, 250–255. [CrossRef]
33. Maratray, F. Choice of appropriate compositions for chromium-molybdenum white irons. *AFS Trans.* **1971**, *79*, 121–124.
34. Abdel-Aziz, K.; El-Shennawy, M.; Omar, A.A. Microstructural Characteristics and Mechanical Properties of Heat Treated High-Cr White Cast Iron Alloys. *Int. J. Apll. Eng. Res.* **2017**, *12*, 4675–4686.
35. Doğan, Ö.N.; Laird, G.; Hawk, J.A. Abrasion resistance of the columnar zone in high Cr white cast irons. *Wear* **1995**, *181*, 342–349. [CrossRef]
36. Matsubara, Y.; Ogi, K.; Matsuda, K. Eutectic Solidification of High-Chromium Cast Iron—Eutectic Structures and Their Quantitative Analysis. *Trans. Am. Foundrym. Soc.* **1982**, *89*, 183–196.
37. Ohide, T.; Ohira, G. Solidification of High Chromium Alloyed Cast Iron. *Foundryman* **1983**, *76*, 7–14.
38. Doğan, Ö.N. Columnar to equiaxed transition in high Cr white iron castings. *Scr. Mater.* **1996**, *35*, 163–168. [CrossRef]
39. Filipovic, M.; Romhanji, E.; Kamberovic, Z. Chemical composition and morphology of M7C3 eutectic carbide in high chromium white cast iron alloyed with vanadium. *ISIJ Int.* **2012**, *52*, 2200–2204. [CrossRef]
40. Medvedeva, N.I.; Van Aken, D.C.; Medvedeva, J.E. Stability of binary and ternary M23C6 carbides from first principles. *Comput. Mater. Sci.* **2015**, *96*, 159–164. [CrossRef]
41. Choi, J.W.; Chang, S.K. Effects of Molybdenum and Copper Additions on Microstructure of High Chromium Cast Iron Rolls. *ISIJ Int.* **1992**, *32*, 1170–1176. [CrossRef]
42. Powell, G.L.F.; Laird, G. Structure, nucleation, growth and morphology of secondary carbides in high chromium and Cr-Ni white cast irons. *J. Mater. Sci.* **1992**, *27*, 29–35. [CrossRef]
43. Laird, G. Microstructures of Ni-Hard I, Ni-Hard IV and High-Cr White Cast Irons. *AFS Trans.* **1991**, *99*, 339–357.
44. Carpenter, S.D.; Carpenter, D.; Pearce, J.T.H. XRD and electron microscope study of an as-cast 26.6% chromium white iron microstructure. *Mater. Chem. Phys.* **2004**, *85*, 32–40. [CrossRef]
45. Kagawa, A.; Okamoto, T.; Saito, K.; Ohta, M. Hot hardness of (Fe, Cr)3C and (Fe, Cr)7C3 carbides. *J. Mater. Sci.* **1984**, *19*, 2546–2554. [CrossRef]